UNIVERSITY OF LEEDS

This is a repository copy of *Systematic Analysis of the Coupling Effects within Supported Plasmonic Nanorod Antenna Arrays*.

White Rose Research Online URL for this paper:
http://eprints.whiterose.ac.uk/135465/

Version: Accepted Version

Systematic Analysis of the Coupling Effects within Supported Plasmonic Nanorod Antenna Arrays

Joshua W. Cottom, [*,†] Patricia Abellan, [‡] Quentin M. Ramasse, [†,‡,§] Kevin Critchley, [§] and Rik Brydson [†]

[†] School of Chemical and Process Engineering, University of Leeds, Leeds, LS2 9JT, UK

[‡] SuperSTEM Laboratory, SciTech Daresbury Campus, Daresbury, WA4 4AD, UK

[§] School of Physics and Astronomy, University of Leeds, Leeds, LS2 9JT, UK

ABSTRACT

Vertically aligned gold nanorod arrays (of aspect ratios from 3.0 to 18.0), supported on metal substrates were fabricated by electrochemical deposition within porous anodic aluminum oxide (AAO) templates. However, the coupling effects that occur within these supported arrays are complex, involving both particle-substrate and particle-particle coupling, and far from fully understood. We have performed a systematic investigation into these effects using finite element modeling (FEM) and correlated these results to experiment. We demonstrate that within the strong coupling regime, the optical properties of the arrays are predominantly governed by inter-rod spacing. Additionally, by supporting the arrays on metal films, the absorption efficiency is

significantly enhanced. We explain these coupling effects in terms of plasmon hybridization theory and image charges. We demonstrate that the longitudinal mode may be tuned throughout the visible region and present resonant wavelength contour plots as a function of inter-rod spacing and aspect ratio (AR) as an aid for the design of plasmonic arrays in applications such as photovoltaics and photocatalysis. Finally, we show that coupling within unsupported and supported arrays can redistribute the electric field to either the center or base of the nanorods respectively whilst propagating along the inter-rod axis, which is potentially of interest for optical waveguide applications.

1. INTRODUCTION

It is widely known that the properties of nanostructures can differ significantly from those in bulk form, allowing the realization of new and unique features.[1,2] This is particularly true for noble metal nanoparticles (NP), where their small size in relation to an incident electromagnetic wave can cause the free electrons of the NP to collectively oscillate at a resonant frequency, a phenomenon known as localized surface plasmon resonance (LSPR). Noble metal nanostructures able to sustain LSPRs have received much attention due to their ability to confine radiation at the nanoscale, increase the optical cross section, significantly enhance the local electric field strength, and dictate the wavelength at which these features occur via control of the material, size and environment of the NP.[3] These unique properties make them key to a wide range of applications, including surface-enhanced Raman spectroscopy (SERS), biosensors, waveguides, and in the development of more efficient photocatalytic or photovoltaic devices.[4-9]

Although it has recently been shown dielectric nanoantenna are also capable of producing enhanced local electric field strengths and scattering cross sections without suffering the high losses associated with interband transitions in metal nanoparticles,[10,11] certain applications such as photocatalysis[12] still require this high absorption.

To date, much research has been focused on maximizing the various plasmonic properties listed above by altering the NP geometry or by placing multiple NPs in close proximity (typically less than ca. 100 nm) so that their plasmons are coupled. Nanorods are particularly promising geometries due to their anisotropic properties, with two main plasmonic modes being present relating to oscillations over their width (transverse mode) and length (longitudinal mode). These modes are known to exhibit unique coupling properties when in arrays depending on their relative

orientation and spacing,[13] whereas additionally the longitudinal mode shows high sensitivity to the nanorods aspect ratio, thereby allowing control over the resonant wavelength.

Similarly, aligning nanorods into vertical arrays is also a popular method to achieve plasmon coupling. This is partly due to the ease by which they may be fabricated by electrodepositing metals into the pores of AAO templates resulting in regular arrays of nanorods over large (cm^2) areas, whilst also retaining high levels of control over the diameter, aspect ratio and inter-rod spacing.[14,15] Additionally however, nanorod arrays significantly increase the surface area of a device, providing benefits in practical applications such as photocatalysis.[16] Furthermore, nanorods produced by this method are also typically grown on a metal substrate thereby potentially offering additional substrate coupling,[17,18] although the exact nature of this is often dependent on specifics of the geometry and the illumination conditions.[19] This substrate coupling however still remains an underexplored topic, particularly for metallic substrates and vertically-aligned nanorods.

Understanding the coupling of plasmonic resonances in systems where two or more nanostructures are placed adjacent to each other is highly relevant since it can result in new spectral features and optical phenomena. Although nanorod arrays produced via electrodeposition in AAO templates are relatively popular, the coupling effects within the arrays are complex and poorly understood. While a number of authors have reported the coupling of NPs with metallic films, this has typically been restricted to only a single particle-film interaction.[17,20-22] Similarly, for nanorod antenna arrays, attention has generally only been directed to the particle-particle coupling that occurs within the arrays.[23-25] This is surprising as many fabrication routes (including electrodeposition in AAO templates) produce arrays that are deposited on a thick metal substrate

and therefore have both types of coupling occurring simultaneously; despite this, analysis of these systems has largely been neglected.

In an attempt to better describe how plasmons couple, plasmon hybridization theory was developed.[21,26-28] In an analogous manner to molecular orbital theory, plasmon hybridization theory addresses the hybridization between the plasmonic modes of various nanostructures by deconstructing the complex plasmonic resonances into combinations of much simpler plasmonic resonances related to the constituent nanoparticles. This is performed in such a way that the hybridization of each of these simpler plasmonic resonances describes the overall interaction between the nanostructures, as well as the energy at which each interaction occurs. To date, notable uses of plasmon hybridization theory include the coupling of a nanoparticle with a metallic substrate[21] as well as the coupling within a nanorod dimer,[28] the results of which serve as a basis for the interpretation of significantly more complex structures, such as the supported nanorod arrays studied in this work.

In regards to supported nanorod arrays, much of the current work has investigated their properties via a combination of experimental measurements and finite element modeling (FEM). [23,24,29-32] These studies typically produce the arrays in AAO templates using a thin-film method, whereby the substrate is optically transparent (<10 nm thick) so that UV-Vis transmission measurements may be acquired. Here, the effects of the substrate are often neglected for simplicity, therefore their conclusions cannot be transferred to arrays produced with much thicker substrates where coupling between adjacent nanorods and the substrate is also believed to occur. This work aims to address this shortfall by systematically investigating the coupling effects within supported plasmonic nanorod antenna arrays by FEM, both in terms of particle-particle coupling and particle-substrate coupling. FEM results are compared to experimental results for validation as required.

Lastly, the results are summarized in contour plots, which are intended to provide a practical design tool for the fabrication of plasmonic nanorod antenna arrays for photovoltaic and photocatalysis applications whereby maximizing and controlling the absorption within the visible region is paramount.[33]

2. EXPERIMENTAL SECTION

2.1 Simulations

All finite element modeling (FEM) simulations were undertaken in the frequency domain using the Comsol Multiphysics 5.2a software package with the additional radio frequency (RF) module. The refractive index for gold, silver and copper was obtained from the experimental data of Johnson and Christy.[34] The diameter of the gold nanorods was 30 nm in all simulations with varying ARs depending on the specific simulation. In order to excite the nanorods longitudinal mode, simulations were performed assuming a p-polarized incident plane wave with either a 45° or 20° angle of incidence (AOI). The geometry, including all media and boundary conditions used for the simulations, together with the details of the two-step approach used to calculate the absorption cross section, can be found in the supporting information (SI) and Figure S1.

2.2 Fabrication

The fabrication of the gold nanorod arrays was based around the initial production of highly ordered porous anodic aluminum oxide (AAO) templates using a two-step anodization method.[35,36] The geometrical parameters of this template were regulated by controlling the anodizing conditions, before subsequently removing the insulating barrier layer and thermally evaporating a

150 nm film of gold onto the template base to form a working electrode for each pore. Electrodeposition of gold within the pores at a constant potential of -0.92 V relative to an Ag/AgCl reference electrode then produced ordered and supported nanorod arrays whereby the length of the nanorods was assessed by monitoring the charge passed. Either the substrate or the alumina template was then selectively etched to leave unsupported nanorod arrays in AAO, or supported nanorod arrays in air, respectively. Further details of the methodology are discussed in the SI.

2.3 Experimental Measurements

The uniformity and dimensions of the fabricated nanorod arrays were assessed in a Hitachi SU8230 scanning electron microscope (SEM). UV-Vis measurements at 0° and 20° AOI were then undertaken on unsupported nanorod arrays in AAO due to the lack of a substrate allowing light transmission. A Perkin Elmer 1050 UV-Vis equipped with a 150 mm integrating sphere and variable angle sample holders was used, acquiring over the wavelength range of 400-800 nm in both s- and p-polarization, as set by means of a Glan-Thompson polarizer supplied by Perkin Elmer.

Electron energy loss spectroscopy (EELS) measurements were performed on thin cross-sections of the array, prepared for electron transparency by ion beam thinning using a Gatan precision ion polishing system (Gatan Model 623) until a thickness of 100 nm was reached. This thinning process led to partial areas of the substrate being removed, thereby allowing the characterization of both unsupported and supported nanorods by EELS. The sample was first baked in vacuum conditions for 12 hours as 50°C before subsequently acquiring EELS measurements using a Nion UltraSTEM 100MC "Hermes" aberration-corrected scanning transmission electron microscope (STEM) with a monochromated electron source. All EELS

measurements were acquired using an accelerating voltage of 60 kV, an energy dispersion of 0.01 eV/channel, and convergence and collection angles of $\alpha = 31$ mrad and $\beta = 44$ mrad, respectively. Further details of the methodology for the experimental measurements can be found within the SI.

3. RESULTS AND DISCUSSION

To analyze the complex coupling effects within supported nanorod antenna arrays, the plasmonic modes of the system were simulated using FEM models. Each plasmonic mode was deconstructed into the separate components by considering the individual coupling mechanisms of simpler independent resonators. These included: (1) the coupling effects between a single gold nanorod and a substrate, (2) the coupling effects for unsupported side-by-side arrays of nanorods, and finally (3) the supported nanorod antenna array. For each of the supported geometries, the gold nanorods were arranged vertically on the substrate thereby replicating the structures produced by electrodeposition within AAO templates.

3.1 Substrate Coupling

Although template-assisted electrodeposition requires the use of conductive substrates to perform as working electrodes, the simulations presented here considered both a variety of conductive metals (gold, silver and copper) as well as a dielectric substrate with refractive index $n_b = 1.5$ (i.e. glass), due to the latter also widely being used in other fabrication procedures.[37,38] The supported nanorods (Figure 1a) had a constant AR of 3.0, however, these results were further compared to unsupported nanorods in a homogeneous medium ($n_a = 1.0$) with ARs of both 3.0 and 6.0 (Figure 1b). Since the incident electric field was p-polarized and had an AOI of 45°, both the transverse and longitudinal modes of the nanorods were excited, although the former was relatively weak and therefore difficult to resolve.
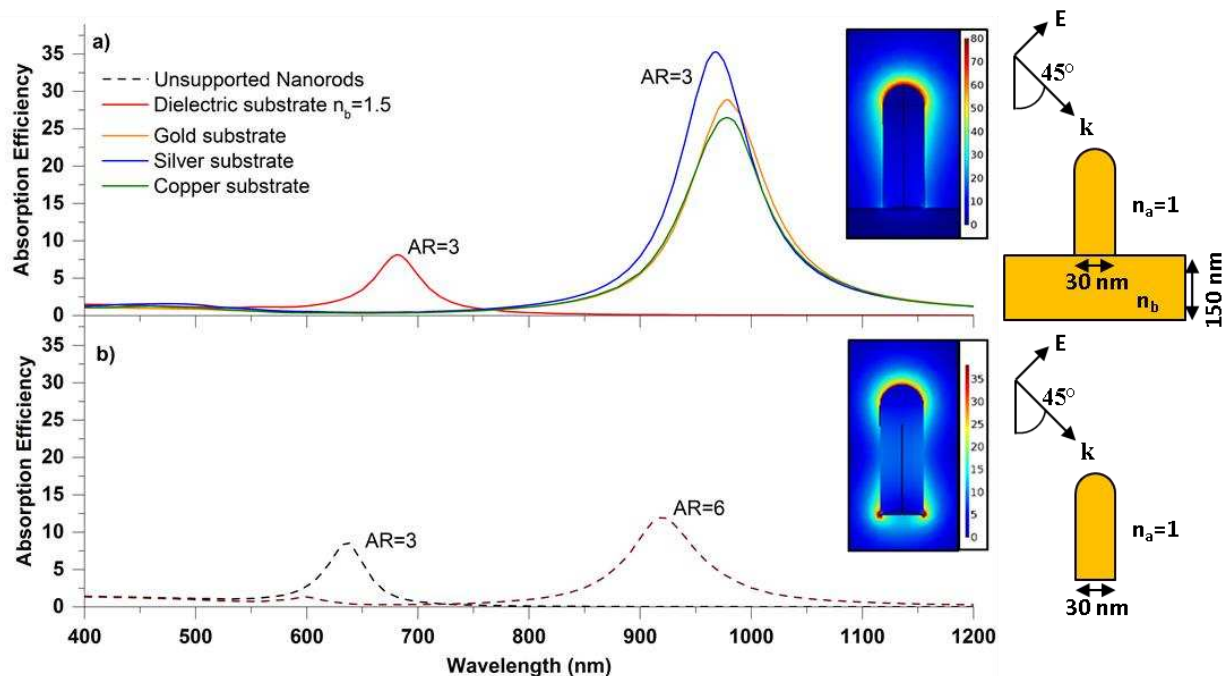
Figure 1: Absorption efficiency for a) a supported Au nanorod of AR = 3.0 on various substrate materials, and b) an unsupported Au nanorod of AR = 3.0 and 6.0. The insets show the normalized electric field plot for an AR = 3.0 nanorod supported on a gold substrate at a wavelength of 979 nm, and an AR = 3.0 unsupported nanorod at a wavelength of 636 nm.

Figure 1 reveals that a substrate has a large effect on both the resonant wavelength of the longitudinal mode and the amplitude of the absorption efficiency, as compared to the corresponding unsupported nanorod. Both the dielectric and metallic substrates lead to a red-shift of the longitudinal mode resonance position. This is most prominent for the metal substrates whereby a dramatic shift of ca. 340 nm occurs as compared to just 46 nm for the dielectric substrate. Furthermore, the metallic substrates also give a large enhancement in the absorption efficiency, with a factor of three to four increase observed dependent on the metal.

The change in absorption efficiency is also apparent in the background electric field plots shown in Figure S2 in the SI. Compared to the vacuum solution, the reflective gold substrate results in a standing wave above its surface with a superposition of the incident and reflected waves

combining to give increased electric field strength. We therefore propose that the substrate impacts on the amplitude of the absorption efficiency by altering the local electric field strength surrounding the nanoparticle, in agreement with the work of Lermé et al.[39]

In contrast, the degree of red-shift evident in the simulations can be explained by alternative theories. Firstly, the small red-shift noted for the dielectric substrate arises due to the change in the permittivity of the local environment. The Frölich condition states that for a small or slowly varying imaginary permittivity, the resonance occurs when $\varepsilon'(\omega) = -2\varepsilon_m$, where $\varepsilon'(\omega)$ is the real part of the nanoparticle permittivity and ε_m is the permittivity of the medium. For a metal nanoparticle described by the Drude model, this implies a red-shift with increasing permittivity of the medium. For the gold substrate, however, the real part of its permittivity is negative and therefore this theory does not explain the dramatic red-shift observed. Instead, this can be explained by strong coupling between the nanorod and the substrate as described by the image charge method.[36]

The image charge method is an analytical concept used to solve the problem of a charge above a conducting planar surface by specifying an opposite imaginary charge at an equal but negative distance away from the interface. As seen in the inset of Figure 1a, the longitudinal mode of the supported nanorod has a monopole-like distribution of its electric field instead of the typical dipolar distribution in unsupported nanorods (e.g. inset of Figure 1b), suggesting that the nanorod may indeed behave as it were coupling with an imaginary charge within the substrate. Furthermore, as the nanorod is directly on the substrate, the image charge method would suggest that this imaginary charge should be located a distance below the substrate surface equal to the height of the nanorod, thereby equivalent to a nanorod that is twice as long (i.e. AR = 6.0). Indeed, there is reasonable agreement between the resonance positions of the AR = 3.0 nanorod supported on a

metallic substrate and that of an unsupported AR = 6.0 nanorod in vacuum, although the former is marginally red-shifted. This difference may perhaps be explained by the simulations accounting for the interaction of higher order multipolar modes, in contrast to that of the image charge method which only assumes dipole-dipole coupling.[40] Further simulations with different AR nanorods (Figure S3 in the SI) show the same trend thereby supporting this hypothesis. Additionally, the resonant wavelengths of the nanorods supported on metallic substrates were seen to be fairly insensitive to the specific metal involved suggesting that the metallic substrates primarily act as a conducting surface and do not contribute to the plasmonic resonance in a manner one might expect of a bimetallic nanorod.

In practical terms, these results demonstrate that placing the nanorods on a metallic substrate provides an important advantage in that the absorption efficiency is significantly enhanced and not only exceeds that of unsupported nanorods of similar AR, but in fact surpasses that of an unsupported nanorod of double the AR. This may prove beneficial for the production of regular arrays of nanorods, including those produced by electrodeposition within AAO templates. This is due to an inherent problem with the fabrication method whereby longer AR nanorods have a tendency to coalesce at their unsupported ends, thus disrupting the periodicity. [41] By utilizing supported nanorods with a shorter AR this agglomeration may be avoided, whilst still achieving high levels of absorption. The large red-shift seen with supported nanorods may also prove useful for achieving absorption within the near infra-red (NIR) region, such as for ex-situ bio-applications that require the absorption of light to be tuned to within the NIR tissue transparency window.[42]

To validate experimentally that the presence of a gold substrate leads to large red-shifts in resonant wavelength, a gold nanorod array was fabricated on a 150 nm thick gold substrate using the AAO electrodeposition method. Part of the array was converted into a 100 nm thick TEM cross

section (as outlined in section 2.3) and EELS measurements were conducted on two regions representative of both supported and unsupported nanorods embedded in AAO. Although the conversion of the nanorod array into a TEM cross section may have implications on the coupling and optical properties, these alterations are believed to be minimal based on the nanorods having a much smaller diameter (30 nm) than that of the cross-section thickness (100 nm). The EEL spectra are shown in Figure 2a whereas the corresponding high angle annular dark field (HAADF) images and EELS integrated intensity maps are shown in Figure 2b.
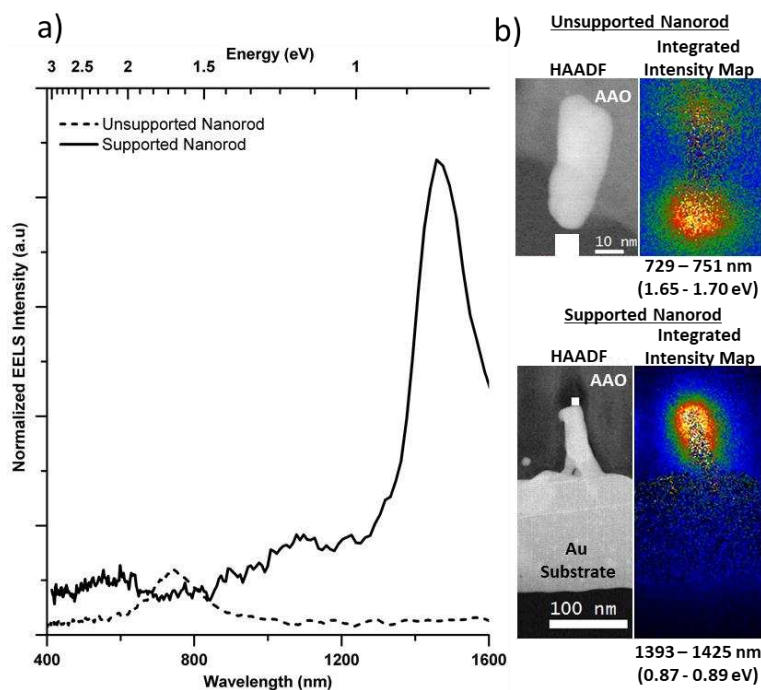

Figure 2: a) Experimental EELS spectra for an unsupported nanorod, and a supported nanorod on a 150 nm thick Au substrate. Both the unsupported and supported nanorods are Au, embedded in AAO, and have similar aspect ratios of 2.8 and 3.2 respectively. b) HAADF images of both nanorods alongside integrated intensity maps visually showing the locations of electron energy loss. Spectrum images were generated by serially rastering the probe across the areas shown in the above images, with a spectrum acquired at each point. Each EEL spectrum represents an integration over an 8 nm × 8 nm area as shown by the white boxes in the HAADF images, located directly adjacent to the end of the nanorods. Normalization of the spectra and integrated intensity maps was performed based on the total electron counts over the entire energy range to account for the inhomogeneity between the vacuum and AAO backgrounds. The data analysis for EELS is discussed in more detail within the SI.

The unsupported nanorod exhibits a peak at ca. 750 nm (1.65 eV) relating to the longitudinal mode of the nanorod. Although this is slightly red-shifted as compared to that expected for an AR = 2.8 nanorod, this can be attributed to it being largely embedded within a high refractive index AAO medium. Although, the supported nanorod is also embedded in AAO and had a comparable AR of 3.2, its longitudinal mode is significantly red-shifted to ca. 1450 nm (0.86 eV) and exhibited a much greater normalized EELS intensity. Both observations can be attributed to nanorod-substrate coupling as predicted by the simulations.

To further investigate the nanorod-substrate interaction, the modeling results for an unsupported gold nanorod dimer (Figure 3a) are compared to a gold nanorod located at different distances above an infinite gold substrate (Figure 3b). Although inter-object gap sizes of 3 nm and 1 nm are included in the results, it should be noted that the model does not take into account non-local effects, which are known to become important for distances below 5 nm.[43] Despite this limitation, the assumption of purely local effects again becomes valid at a gap size of 0 nm, where the systems are modeled as one continuous structure.
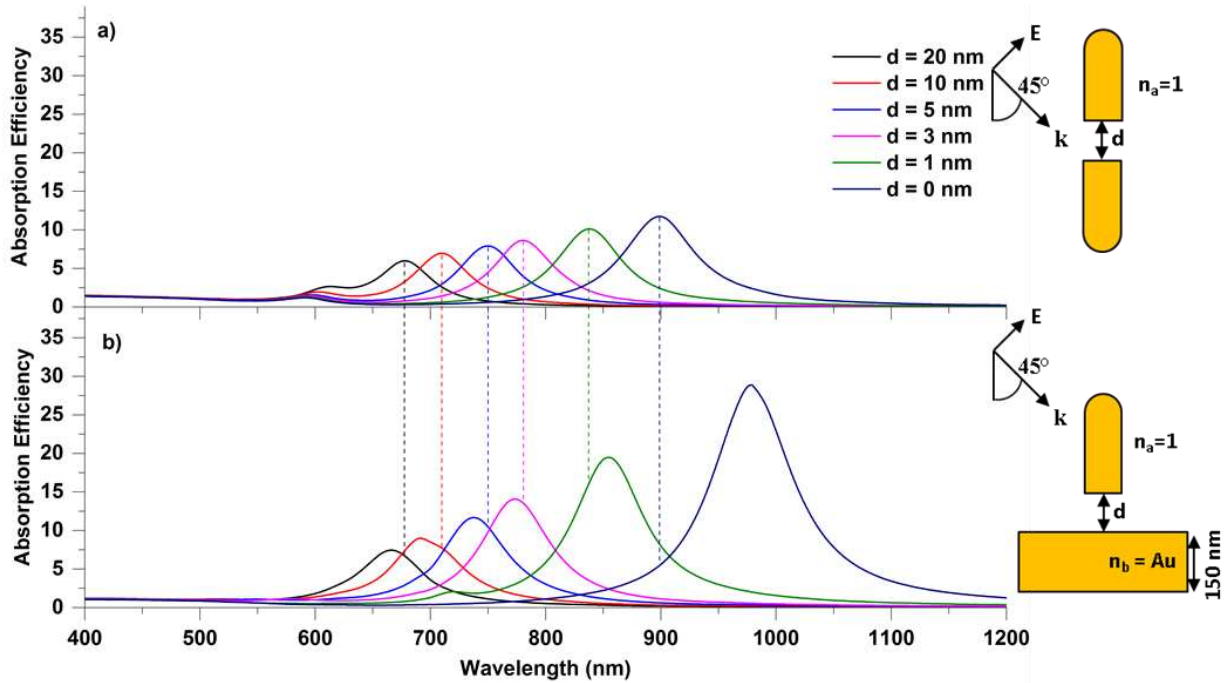
Figure 3: Absorption efficiency for a) an unsupported Au nanorod dimer and b) an Au nanorod above an Au substrate, for varying gap size, d. The nanorods have a diameter of 30 nm and an AR = 3.0. The vertical dashed lines act as a guide to visualize the relative peak positions for each gap size.

Figure 3 shows that as the gap size (d) is reduced, a red-shift and an increase in absorption efficiency occurs both for the dimer and nanorod-substrate scenarios. This occurs in an exponential manner with only gradual changes at large distances and much greater variations as the spacing is reduced and the coupling strength increased. The increase in absorption efficiency at small gap sizes is also more significant for the nanorod-substrate combination relative to the nanorod dimer, suggesting that the substrate also enhances the local electric field strength.

Comparing the nanorod dimer and nanorod-substrate scenario results, reveals that the resonant wavelengths generally match reasonably well, except for the case of a 0 nm gap (i.e. an unsupported nanorod of AR = 6.0 and a supported nanorod of AR = 3.0), which as already noted in Figure 1, shows the supported nanorod being slightly red-shifted in comparison to the double

AR nanorod. Despite this, the similarity between the results once again supports the conclusion that the presence of a substrate leads to the formation of an image charge.

Interestingly, the dimer spectra shown in Figure 3a also show the presence of a second peak at a wavelength of ca. 600 nm for all separations. For a 0 nm gap (i.e. a single nanorod of AR = 6.0), the charge distribution map reveals that this is a quadrupolar mode, excited due to the non-normal AOI of light. However, as the gap size increases creating a nanorod dimer, this mode persists and is instead believed to be related to the lower wavelength anti-bonding dark mode of an end-to-end nanorod dimer, which, as found by Osberg et al.[44] bears similarities to the quadrupolar mode of a discrete nanorod. We suggest that the reason why this mode is absent in the spectra of Figure 3b is due to the fact that the substrate image charge method is required to be an equal but negative distance away from the substrate surface and of the opposite charge. This therefore prevents the formation of an image antibonding mode where the charge polarization is anti-symmetric, as shown schematically in Figure S4 of the SI.

To conclude the modeling of a nanorod on a substrate, the effect of the substrate thickness was investigated, as shown in Figure 4a. The substrate thickness was increased from 0 nm (i.e. an unsupported nanorod) up to 150 nm. Firstly, the simulated spectra for substrate thicknesses of 100 and 150 nm are equivalent, indicating that for thick substrates (t >100 nm), the resonant wavelength and absorption efficiency both plateau and the spectra become invariant. For very thin substrates (1-5 nm thick), a resonance around 600 nm is observed which is blue-shifted relative to the longitudinal mode of the individual nanorod and reduces with increasing substrate thickness. Additionally, a second peak at much higher wavelength emerges with the opposite trend. Here, the substrate thicknesses of 1 nm and 2 nm are red-shifted and broadened to an extent that they are not clearly identifiable; however, as the thickness increases to 3nm and above, this higher wavelength

peak subsequently blue-shifts and amplifies. By a thickness of 10 nm, this higher wavelength peak becomes dominant and the lower wavelength peak disappears.

Interestingly, a number of weaker peaks are also present at thin substrate thicknesses, such as that seen at approximately 1200 nm for a thickness of 2 nm. These peaks are believed to be related to the onset of higher order modes due to the coupling between the substrate and nanorod.
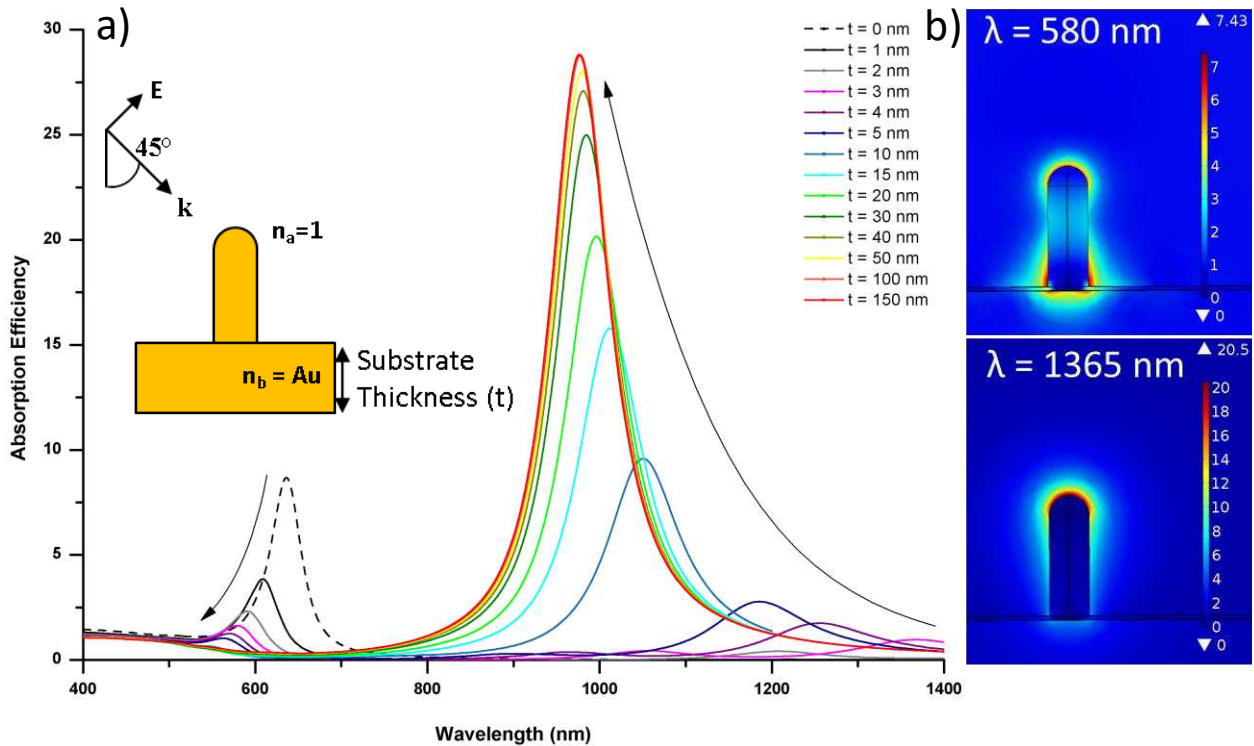

Figure 4: a) Absorption efficiency spectra for a gold nanorod of AR = 3.0 supported on a gold substrate of varying thickness (t). b) Normalized electric field plots for the nanorod on a 3 nm thick Au substrate at the resonant wavelength of both peaks.

These complex results require a more detailed understanding, which can be achieved by viewing the electric field distribution in Figure 4b. The field distributions for the lower wavelength mode ($\lambda = 580$ nm) resemble that of an unsupported nanorod in that the E-field is located at both

ends of the nanorod in a characteristic dipolar arrangement (similar to the inset in Figure 1b). In contrast, the higher wavelength mode (λ = 1365 nm) appears to instead have a monopole-like distribution (similar to Figure 1a). A number of conclusions can be drawn from these observations: firstly, for relatively large substrate thicknesses, approximately equal to or greater than the height of the nanorod, image charges are valid. However, with a reduction in substrate thickness the validity of the image charge method begins to fail resulting in a splitting of the mode. Here, the higher wavelength peak represents the validity of image charges, whereas the lower wavelength peak reflects the breakdown of this approximation. As the substrate thickness is reduced the image charge method progressively fails, so that the higher wavelength peak weakens whilst the lower wavelength peak strengthens in intensity. The latter may be physically explained by the substrate causing less damping of the oscillations at smaller thicknesses.

In terms of the observed shifts in the two modes, a similar trend to that of the higher wavelength mode has been observed in other work.[32] Despite this, a physical explanation of these shifts was not forthcoming. It is possible that at these small thicknesses the observed shifts are related to a breakdown in the validity of the model due to the local approximations on which it is based. Future work using a non-local model would therefore be useful in clarifying this point.

3.2 Particle Coupling

Following on from the analysis of the coupling between a single nanorod and a substrate, the effects of coupling between multiple unsupported nanorods were considered. In these simulations nanorods were oriented side-by-side, whereby the long-axes of the nanorods were perpendicular to the inter-particle axis, representing nanorods grown within AAO templates.

17

Figure 5 demonstrates the transition from a finite number of nanorods to a periodic array of nanorods for two different inter-rod spacings. Here the spacing was defined from the edge of one nanorod to the edge of an adjacent nanorod, as shown in the accompanying schematic diagram for a nanorod dimer.
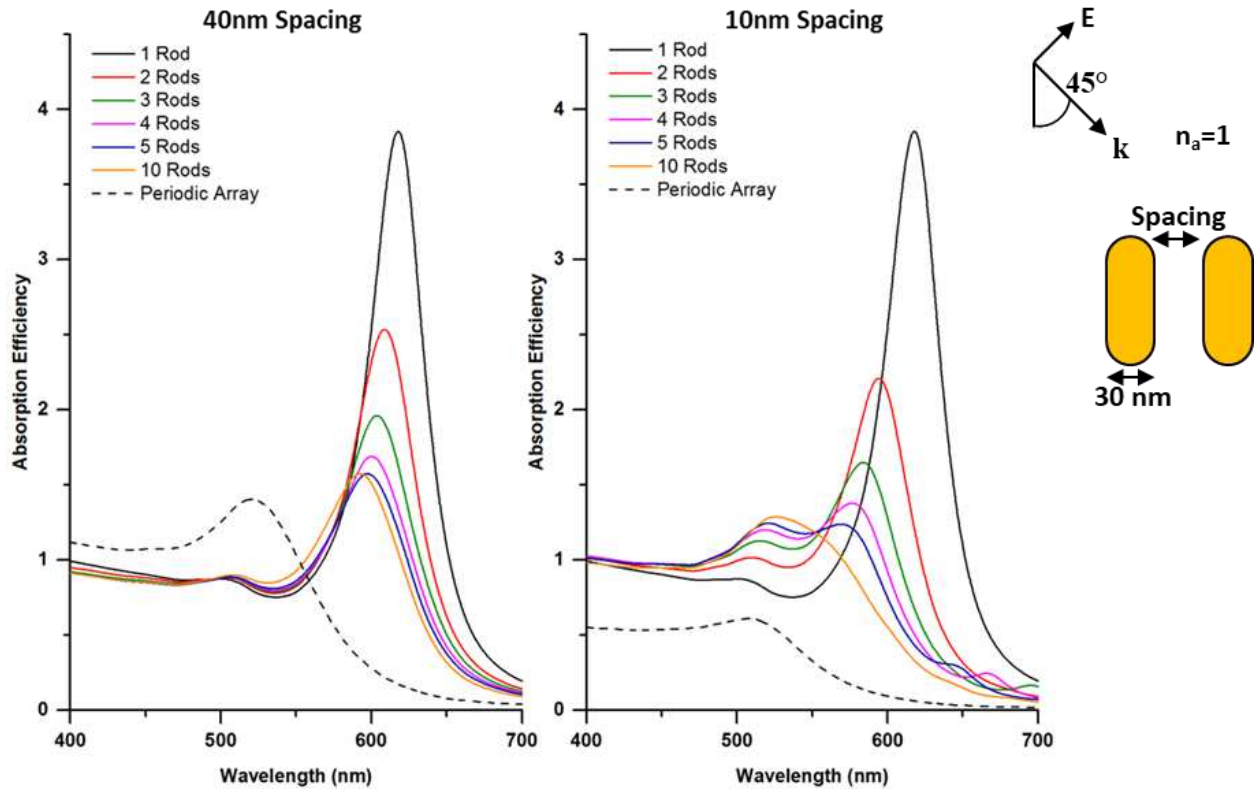

Figure 5: Effect of number of interacting nanorods on the absorption efficiency for an array of side-by-side aligned gold nanorods of AR = 3.0 and diameter 30 nm, excited using p-polarised light at 45°. The periodic array curve represents that of an infinite array of gold nanorods achieved by using Floquet boundary conditions.

Figure 5 shows that as the number of nanorods within a side-by-side aligned nanorod array increases, the longitudinal mode blue-shifts and decreases in absorption efficiency, whereas in contrast the transverse mode red-shifts and increases in absorption efficiency, albeit only slightly. For a spacing of 40 nm these spectral shifts are relatively small, however, at 10 nm spacing they

are much more pronounced resulting in the longitudinal mode beginning to overlap with that of the transverse mode for a set of 10 interacting nanorods.

As seen in the previous section, the dependence on spacing is due to the coupling strength increasing at smaller separations. Similarly, as the number of nanorods in the array increases, the coupling strength likewise increases, leading to shifts in the spectra.[45] The large blue shift of the longitudinal mode and smaller red-shift of the transverse mode also match those predicted by the plasmon hybridization theory for side-by-side nanorods.[28] However, it should be noted that only the optically active bright modes are seen in the present simulations due to the incident plane wave homogeneously exciting the nanorods thereby restricting the nanorods to have symmetric dipoles. Lastly, the change in absorption efficiency was found to be related to the electric fields combining either constructively (transverse modes) or destructively (longitudinal modes),[25] which is also shown in Figure S5 of the SI.

Figure 5 also shows that when transitioning from a finite number of nanorods to an infinite periodic array of nanorods, the coupling strength greatly increases leading to the longitudinal mode completely overlapping with that of the transverse mode for both inter-rod spacing values modeled. It was confirmed that this was the only peak present in the spectra by extending the modeled wavelength range up to 3000 nm. Furthermore, it would be expected that if these modes were indeed overlapped for the infinite array, increasing the nanorod AR would red-shift the longitudinal mode into its own distinct peak.[29] This can be seen in Figure 6a for an infinite nanorod array with increasing AR from 3.0 to 18. Here the extinction cross section was determined, instead of the previously used absorption cross section, due to scattering playing a dominant role with higher AR nanorods, and so allowing a comparison to be made to experimental UV-Vis results (Figure 6b).
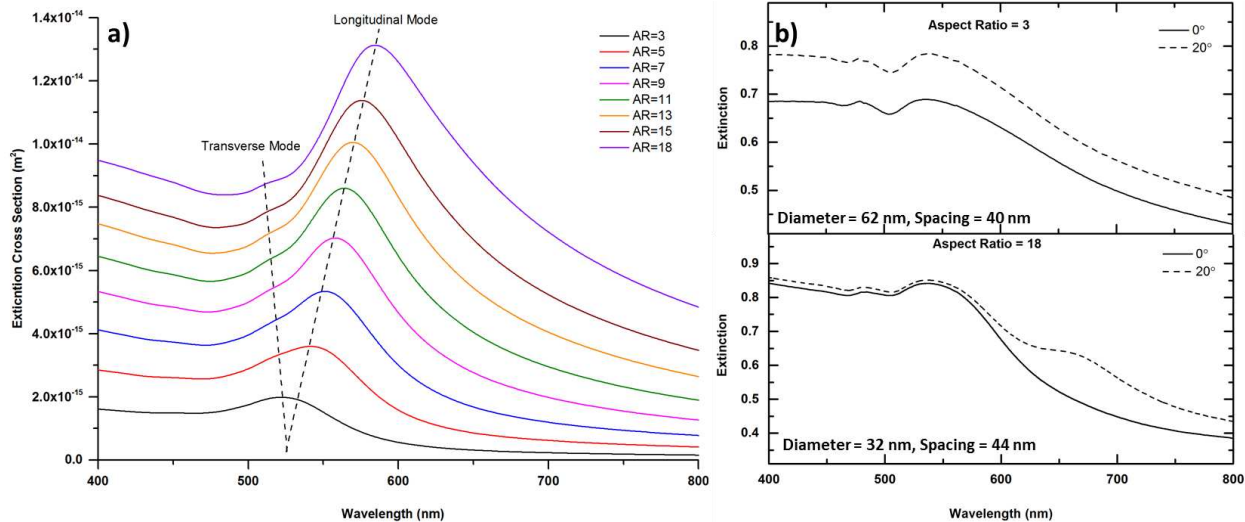
Figure 6: a) Modeling results for an unsupported nanorod array with a diameter of 30 nm, spacing of 40 nm and varying AR. The array was excited by p-polarised light at 20° angle of incidence in a vacuum. b) Experimental UV-Vis results for unsupported nanorod arrays of AR = 3.0 and 18 embedded in AAO. An angle of incidence of both 0° and 20° was used so as to confirm the presence of the longitudinal mode.

For a nanorod array of AR = 3.0 only a single peak is present in the modeled spectra of Figure 6a, however, as the AR is increased the longitudinal mode is seen to emerge and red-shift whereas the corresponding transverse mode blue-shifts slightly, as predicted by Gans theory.[46] These results were further validated by comparing the simulated spectra to experimental UV-Vis spectra of fabricated unsupported nanorod arrays with AR = 3.0 and AR = 18 (Figure 6b). It was seen that the lower AR nanorod arrays have only a single peak at the transverse wavelength, however the longer AR = 18.0 nanorod arrays have a second peak at slightly higher wavelength (~660 nm). We believe that the small peak at 480 nm in each of the spectra is not related to the nanorods but instead arises due to small sections of the substrate being incompletely removed and therefore contributing to the extinction (see Figure S6 in the SI). Furthermore, it was confirmed that no additional peaks were present in the spectra by performing additional scans up to a wavelength of 2000 nm. The higher wavelength peak at 660 nm for the AR = 18.0 nanorod was

validated as the longitudinal mode by performing scans at varying AOI (Figure 6b), and polarization (Figure S7 in the SI), with the peak only being observed for non-normal AOI and p-polarization. General trends between experimental and simulated spectra are similar, however, any disparities can be explained by imperfections in the fabricated sample (variations in diameter, AR and spacing), different embedding media (vacuum or AAO), and scattering effects from the AAO.

Figure 6a shows that the resonance wavelength for a nanorod array is far less sensitive to the nanorod AR than for isolated nanorods. Referring back to Figure 1b, a doubling of the AR from 3.0 to 6.0 led to a ~300 nm red-shift and the resonant wavelength being located outside of the visible region of the spectrum. By contrast, in the side-by-side coupled nanorods of Figure 6a, an increase in AR by a factor of 6 only led to a red-shift of less than 100 nm, with the resonant wavelength still being located within the visible. Practically, this is important as it allows longer nanorods to be fabricated in arrays without incurring the large red-shift typically seen in isolated nanorods. Additionally, specific wavelengths may be more easily targeted due to the resonant wavelength being less sensitive to the often unavoidable variations in the size and shape of fabricated arrays. Lastly, the reduced sensitivity to AR means techniques such as in-situ ellipsometric monitoring of arrays optical properties may be harnessed so that extinction at precise wavelengths may be achieved.[47] This lower reliance on AR, however, is only true in the strongly coupled regime, whereas at larger spacings the rods regain the traits of isolated nanorods. By understanding this inter-relationship between the spacing and the AR of the nanorods, it may be possible to design nanorod arrays with absorption occurring anywhere over visible and near-infrared wavelengths. This is demonstrated by contour plots whereby the resonant wavelength (Figure 7a) and absorption cross section (Figure 7b) of the longitudinal mode are plotted as a function of both the nanorod array spacing and AR. In these simulations the medium was given a

refractive index of n = 1.51 representing the AAO in which they would typically be embedded.[30] It is hoped that these contour plots will help in the design of unsupported nanorod arrays for applications such as photovoltaics and photocatalysis whereby it is often essential to maximize and control the absorption within the visible region.
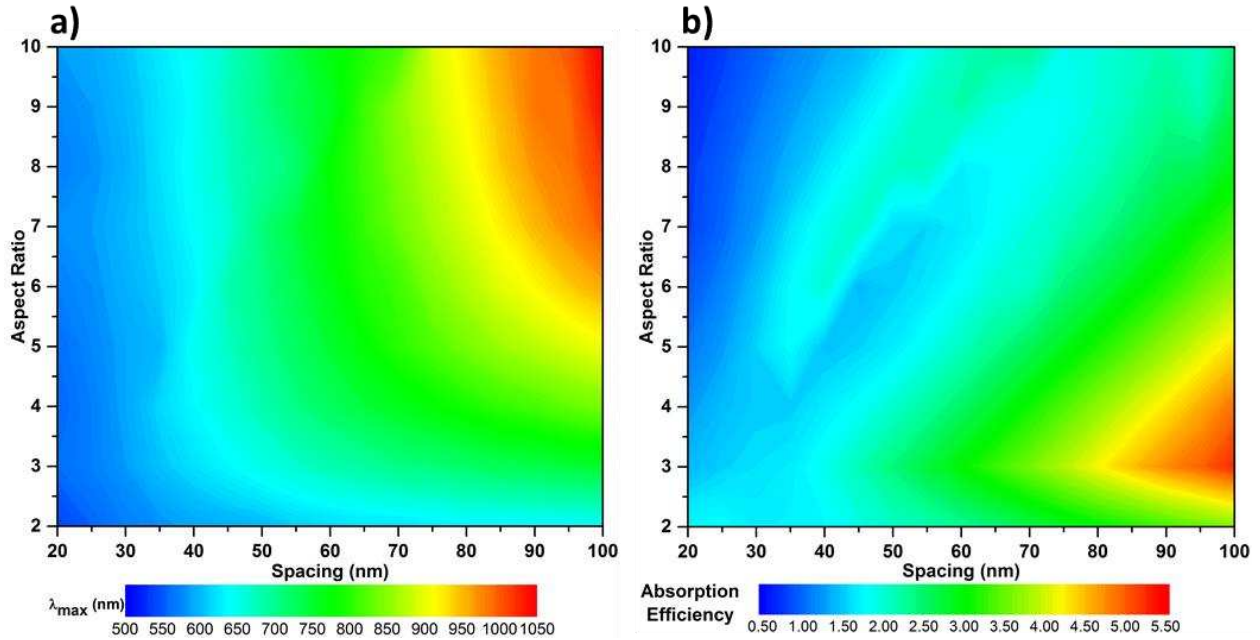

Figure 7: Contour plots of a) lambda max and b) absorption efficiency for unsupported nanorod arrays with spacing and aspect ratio. The nanorods were embedded in AAO (n = 1.51) and p-polarised light at 20° AOI was used.

Figure 7 highlights a number of interesting relationships. For example, the resonant wavelength (λ_{max}) of the longitudinal mode is seen to be fairly insensitive to AR at low spacings, with λ_{max} actually plateauing to a near constant value. In this regime, the spacing of the nanorods dictates the resonant position of the longitudinal mode. Despite this, as the AR of the nanorods is increased, higher order modes (not shown) still become active and subsequently red-shift, eventually also plateauing at the same resonant wavelength as that of the longitudinal mode, and

in so doing, hybridizing together. In this strongly coupled regime, the modes of adjacent nanorods destructively interfere, causing low absorption efficiencies, even at higher ARs.

As the spacing increases, the wavelength at which λ_{max} begins to plateau also increases. Here the arrays begin to show properties more typical of isolated nanorods in that a red-shift with AR once again occurs. Despite this, for the spacings modeled, the red-shift with AR is still significantly smaller than the linear trend typically associated with isolated nanorods. Additionally, the absorption efficiency is found to be maximum at higher spacings. In contrast to isolated nanorods however, the shorter AR nanorods have improved absorption efficiencies compared to the longer AR nanorods. This is attributed to the longer nanorods having stronger dipoles and therefore destructively coupling together even at large spacings.

So far the results have focused on the far-field optical cross-sections of the nanorod arrays, however, it is equally important to understand the near-field properties of the arrays with regards to the distribution of the electric field at the resonant wavelength of the longitudinal mode. Plots of the normalized electric field of an AR = 7.0 periodic nanorod array at the maximum resonant wavelength for different inter-rod spacings are shown in Figure 8a, as compared to an isolated nanorod. Interestingly, it is observed that as the spacing reduces, the electric field distribution alters from being localized around the ends of the nanorod (as for an isolated nanorod), to being located towards the middle of the nanorod. At this lower inter-rod spacing the electric fields are seen to extend right up to the edge of the simulation side boundaries. As these boundaries are periodic this represents the interaction of electric fields associated with adjacent nanorods.
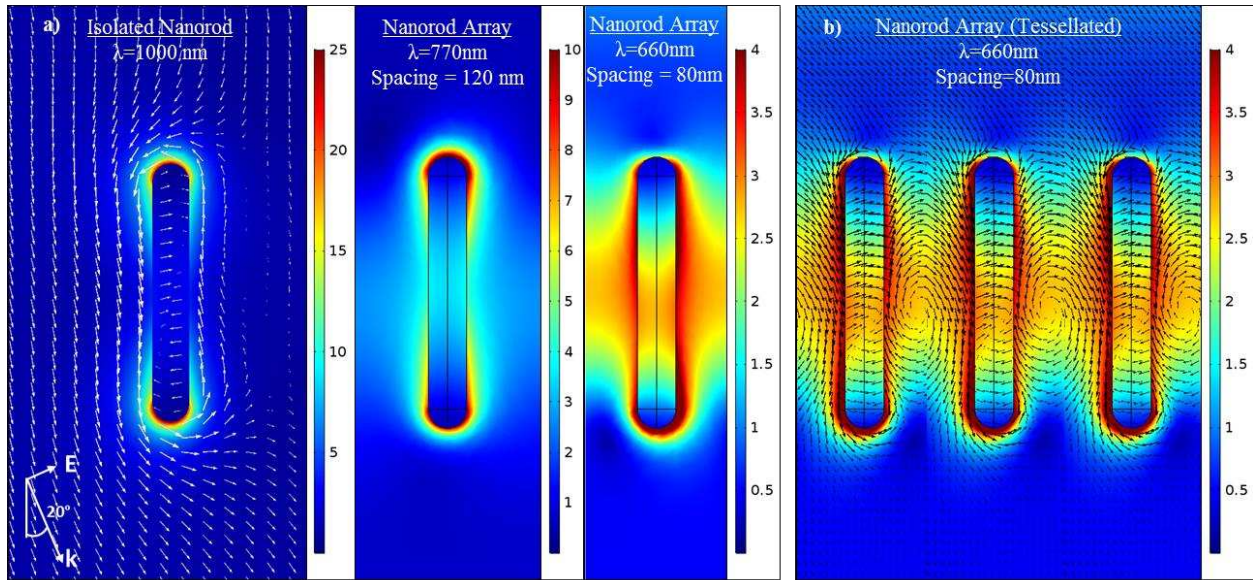
Figure 8: a) Electric field distribution for the longitudinal mode of an isolated and periodic gold nanorod array for two different inter-rod spacings. The nanorods are 30 nm in diameter and AR = 7.0 embedded in a medium with refractive index n = 1.0. The incident light is p-polarized at 20° AOI. b) The horizontal tessellation of the array at 80 nm spacing clearly shows the interaction of the rods. The power flow as shown by the Poynting vector (arrows) is included for the isolated nanorod and the array at a spacing of 80 nm. Any apparent discontinuities at the midpoint between the tessellated nanorods is due to a plotting artefact.

This redistribution of the electric field towards the center of the nanorod array has also been found by a number of other authors[24,31,32] who also proposed that the resulting electric field was able to propagate along the array in a direction parallel to the inter-particle axis, therefore potentially acting as a waveguide. This is supported by the results shown in Figure 8b, whereby the nanorod unit cell was tessellated horizontally and the Poynting vector plotted. Here, it may be seen that the power flow appears to travel along the inter-particle axis of the nanorod array in a wave-like manner.

3.3 Substrate and Particle Coupling

This section considers the case of a periodic nanorod array supported on a thick (150 nm) gold substrate, as is consistent with many fabricated devices produced by electrodeposition within AAO templates. Here we aim to account for coupling of the nanorods with the metallic substrate, and coupling between the nanorods in the array simultaneously. Figure 9 shows simulations for an AR = 3.0 supported nanorod array with an inter-rod spacing of 80 nm. Additional spectra for an unsupported nanorod array, and both a supported and unsupported isolated nanorod of the same dimensions are also included for comparison. Experimental UV-VIS reflectance measurements performed on a bare gold and AR = 9 supported nanorod array are also shown in Figure S6 of the SI. The relatively shallow AOI of 8° used within these reflectance measurements however results in only the transverse mode being clearly visible.
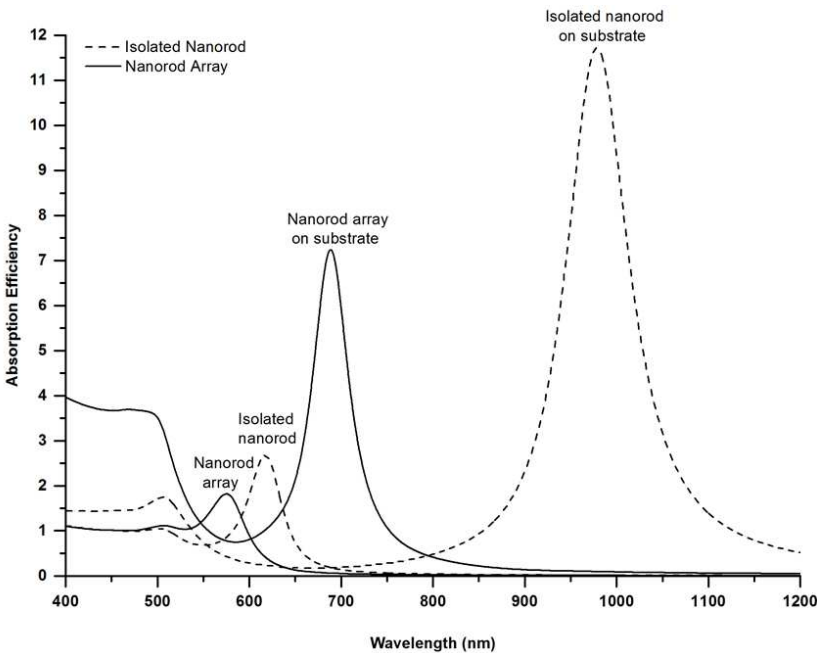

Figure 9: Comparison of absorption efficiency for a periodic array of nanorods (solid lines), in both a homogeneous medium (n = 1.0) and supported on a 150 nm thick gold substrate. Additional dashed lines represent single nanorods not in an array, again either in a homogeneous medium or supported on a gold substrate. P-polarised light at an AOI of 20° was used and the nanorods in the arrays had a spacing of 80 nm and AR = 3.0.

Figure 9 demonstrates that the longitudinal mode of the supported nanorod array is red-shifted relative to that of both an unsupported single nanorod and also an unsupported nanorod array. This confirms previous results suggesting that a large red-shift and an enhancement in absorption efficiency occurs for supported nanorods. On the other hand, the resonant wavelength is seen to be located at a lower wavelength compared to that of a single isolated supported nanorod and to have reduced amplitude. This is due to coupling within the side-by-side nanorod array leading to a blue-shift and decrease in absorption efficiency, as seen previously. We therefore propose that the simultaneous effect of both coupling mechanisms can be approximated as a tradeoff whereby the substrate effectively red-shifts and enhances the longitudinal mode resonant wavelength, whereas the coupling between the nanorods acts to blue-shift and slightly dampen it.

Practically, we believe this result has beneficial implications with regards to achieving a high absorption within the visible spectrum. For instance, by supporting the nanorods on a gold substrate, the absorption efficiency may be greatly enhanced, however, this is at the expense of a large red-shift that will often move the mode out of the visible region, even for very small AR nanorods. This may be compensated by the coupling between the nanorods in the array which acts to blue-shift the resonance back into the visible wavelength, albeit at a slight detriment to the absorption efficiency. Despite this, it was found that by combining both the particle-particle and particle-substrate coupling, the nanorod arrays have a large enhancement to their absorption whilst also still lying within the visible region. This enhancement is seen to occur not only for the longitudinal mode, but also at lower wavelengths below that of the transverse mode.

An added advantage of the supported nanorod arrays over those of isolated nanorods is that the spacing may also be used to control the resonance position. For example, as shown in Figure S8 of the SI, an AR = 3.0 supported nanorod array may have the resonance wavelength of the

longitudinal mode controlled anywhere between 500 nm and 1000 nm by simply controlling the inter-rod spacing. This additional control is not detrimental to the array's absorption properties, with values seen to exceed those of both an AR = 3.0 and AR = 4.0 unsupported single nanorod.

As for unsupported nanorod arrays, contour plots were also constructed for the supported nanorod arrays, plotting λ_{max} (Figure 10a) and the absorption cross-section (Figure 10b) of the longitudinal mode as a function of both the nanorod spacing and AR. These results are for a 150 nm thick gold substrate and the nanorods exposed to vacuum (n = 1.0) (i.e. AAO removed).
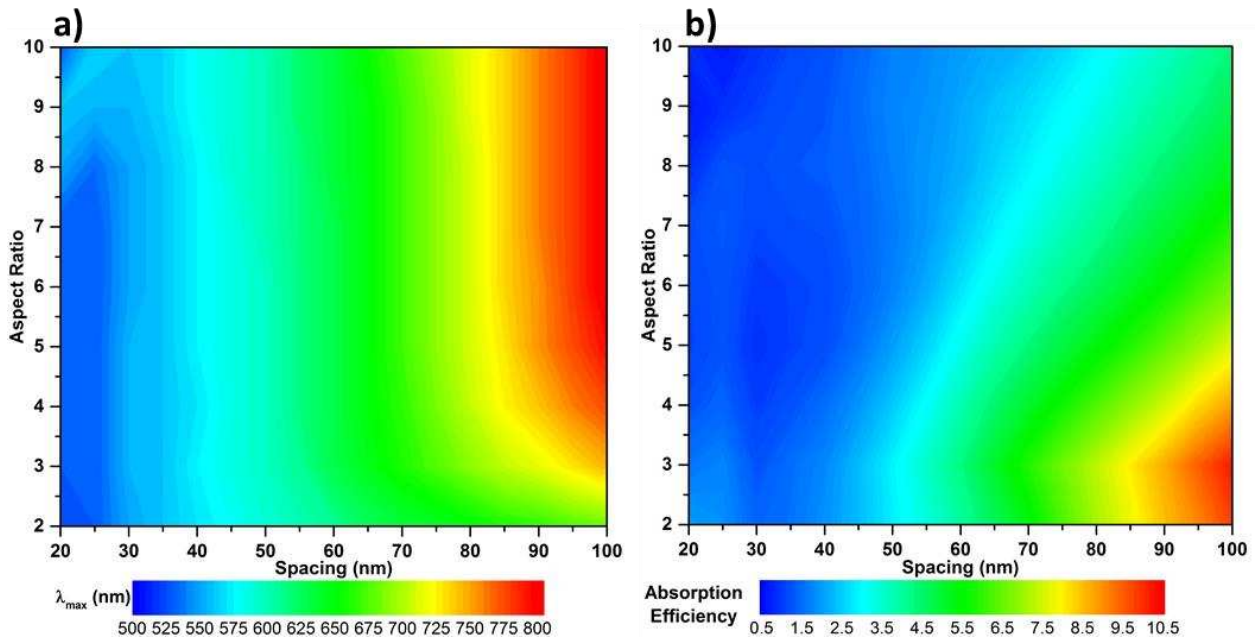

Figure 10: Contour plots of a) lambda max and b) absorption efficiency for supported nanorod arrays with spacing and AR plotting. The nanorods were supported on a 150 nm thick gold substrate, exposed to vacuum (n = 1.0), and p-polarised light at 20° AOI was used.

Figure 10 shows similar trends to those described for the unsupported nanorod array contour plots in that the inter-rod spacing largely dominates the resonant position of the

longitudinal mode. Similarly, λ_{max} was seen to plateau with increasing nanorod AR, with once again the highest absorption efficiencies occurring for large spacings and small ARs due to minimization of destructive interference. These maximum absorption efficiencies are seen to exceed values of 10, thereby doubling those of the unsupported nanorod arrays.

To conclude the analysis of supported nanorod arrays, once again the near field was studied. This is shown in Figure 11a for both a supported isolated nanorod and a supported nanorod array of AR = 7.0 for two different inter-rod spacings. As with the unsupported nanorod array, the electric field distribution of supported nanorods differ greatly when placed within an array. For supported nanorod arrays, the electric field changes from being located at the top of the isolated nanorod, to being increasingly concentrated towards the base of the nanorod array as the spacing between the nanorods is reduced. Additionally, the electric fields in this strongly coupled scenario were seen to extend horizontally along the top of the substrate right up to the simulation boundary thereby once again representing the interaction between adjacent nanorods. Similarly, by studying the Poynting vectors it was also seen that the power flow appears to travel along the nanorod array in a direction parallel to the inter-particle axis (Figure 11b). This novel result once again shows the potential of using supported nanorod arrays in waveguide applications.
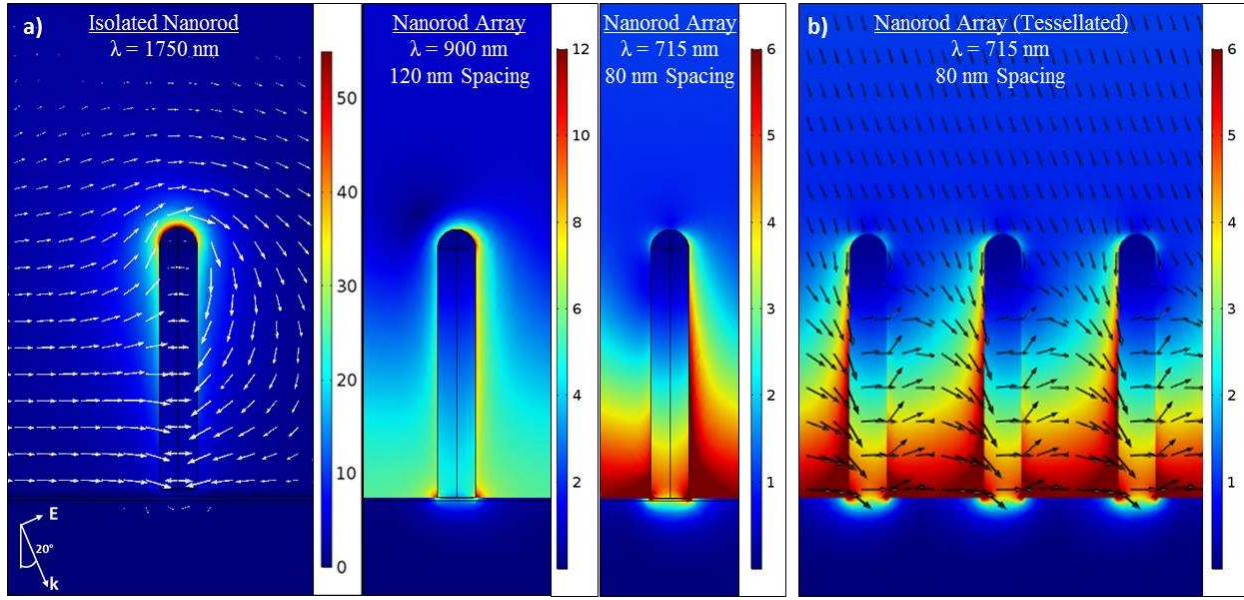
Figure 11: a) Electric field distribution for the longitudinal mode of an isolated and periodic supported gold nanorod array with spacing. The nanorods are 30 nm in diameter, AR = 7.0, and the substrate is gold and 150 nm thick. The incident light is p-polarized at 20° angle of incidence. b) The horizontal tessellation of the array at 80 nm spacing clearly shows the interaction of the rods. The power flow as shown by the Poynting vector (arrows) is included for the isolated nanorod and the array at a spacing of 80 nm. Any apparent discontinuities at the midpoint between the tessellated nanorods is due to a plotting artefact.

The difference between the electric field distributions of the unsupported and supported nanorod arrays, whereby the former concentrates at the center of the nanorod and the latter maximizes at the base, may be intuitively understood in light of our previous findings for supported single nanorods. Namely, the substrate has been shown to essentially act as a mirror whereby the supported nanorods inherit trends similar to unsupported nanorods of twice their AR. Hence if unsupported nanorod arrays have their electric fields concentrated towards the center, the supported nanorod arrays would be expected to redistribute the field towards their base.

4. CONCLUSIONS

The coupling effects within supported plasmonic nanorod antenna arrays have been systemically investigated by finite element modeling and verified experimentally. For the case of individual nanorods coupling to a metallic substrate, it was found that the substrate acts as a mirror whereby the resulting spectra match that of an unsupported nanorod with twice its aspect ratio. This results in a large red-shift and a significant enhancement of the absorption efficiency as compared to an unsupported nanorod of equal size.

Alternatively, for the case of coupled unsupported nanorods in a side-by-side arrangement, the longitudinal mode was found to blue-shift and decrease in absorption efficiency. For strong coupling regimes, the longitudinal mode overlaps with the transverse mode, however, with increasing AR this red-shifts into a distinct peak. Despite this, a much lower sensitivity to AR was observed, with instead the inter-rod spacing largely dictating the resonant wavelength, therefore allowing any dispersion in the ARs of real systems to be accommodated when targeting specific wavelengths.

When these arrays are combined with a metal substrate, both types of coupling are found to compete resulting in a hybridization. The supported nanorod antenna arrays are found to not only have absorption efficiencies exceeding those of unsupported nanorods, but also have resonant wavelengths within the visible spectrum. As supported nanorod arrays can be fabricated both cheaply and easily within AAO templates, whilst also allowing for great flexibility in regards to the spacing, nanorod size, and deposition area, they therefore present promising options for the development of new novel devices. To aid in this, contour plots of the longitudinal modes resonant wavelength and absorption efficiency have also been produced for both supported and unsupported

arrays showing the interconnectivity between the aspect ratio and inter-particle spacing, thereby providing a design tool for practical applications such as photovoltaics and photocatalysis.

Lastly, it was found that the coupling within the arrays leads to a redistribution of the electric field to either the center or base of the nanorods for unsupported and supported arrays respectively, with fields propagating along the array in a direction parallel to the inter-rod axis. Further details of these modes will be discussed in a forthcoming paper, in addition to a detailed analysis of the bright and dark modes within the array observed in experimental EELS data.

5. ACKNOWLEDGEMENTS

6. SUPPORTING INFORMATION

Further details are given on the simulation, fabrication and EELS methodology. Additionally, plasmonic modes of a nanorod dimer and nanorod above substrate, interference in nanorod arrays,

reflectance measurements, UV-Vis measurements with polarization, and supported gold nanorod arrays with spacing are included.

7. REFERENCES

1. Rogers, B.; Adams, J.; Pennathur, S. *Nanotechnology: Understanding small systems, third edition*; CRC Press: Boca Raton, FL, 2014.
2. Ramsden, J. *Nanotechnology: An introduction*; Elsevier Science: New York, 2016.
3. Maier, S. A. *Plasmonics: Fundamentals and applications*; Springer Science + Business Media LLC: New York, 2007.
4. Crozier, K. B.; Zhu, W.; Wang, D.; Lin, S.; Best, M. D.; Camden, J. P. Plasmonics for surface enhanced raman scattering: Nanoantennas for single molecules. *IEEE J. Sel. Top. Quantum Electron.* **2014**, *20*, 152-162.
5. Homola, J. Surface plasmon resonance sensors for detection of chemical and biological species. *Chem. Rev.* **2008**, *108*, 462-493.
6. Gramotnev, D. K.; Bozhevolnyi, S. I. Plasmonics beyond the diffraction limit. *Nat Photon* **2010**, *4*, 83-91.
7. Atwater, H. A.; Polman, A. Plasmonics for improved photovoltaic devices. *Nat. Mater.* **2010**, *9*, 205-213.
8. Xiao, M. D.; Jiang, R. B.; Wang, F.; Fang, C. H.; Wang, J. F.; Yu, J. C. Plasmon-enhanced chemical reactions. *J. Mater. Chem. A* **2013**, *1*, 5790-5805.
9. Warren, S. C.; Thimsen, E. Plasmonic solar water splitting. *Energy Environ. Sci.* **2012**, *5*, 5133-5146.
10. Caldarola, M.; Albella, P.; Cortés, E.; Rahmani, M.; Roschuk, T.; Grinblat, G.; Oulton, R. F.; Bragas, A. V.; Maier, S. A. Non-plasmonic nanoantennas for surface enhanced spectroscopies with ultra-low heat conversion. *Nat. Commun.* **2015**, *6*, 7915.
11. Albella, P.; Poyli, M. A.; Schmidt, M. K.; Maier, S. A.; Moreno, F.; Sáenz, J. J.; Aizpurua, J. Low-loss electric and magnetic field-enhanced spectroscopy with subwavelength silicon dimers. *J. Phys. Chem. C* **2013**, *117*, 13573-13584.
12. Christopher, P.; Xin, H.; Linic, S. Visible-light-enhanced catalytic oxidation reactions on plasmonic silver nanostructures. *Nat. Chem.* **2011**, *3*, 467.
13. Weber, D.; Albella, P.; Alonso-González, P.; Neubrech, F.; Gui, H.; Nagao, T.; Hillenbrand, R.; Aizpurua, J.; Pucci, A. Longitudinal and transverse coupling in infrared gold nanoantenna arrays: Long range versus short range interaction regimes. *Opt. Express* **2011**, *19*, 15047-15061.
14. Foss, C. A.; Hornyak, G. L.; Stockert, J. A.; Martin, C. R. Template-synthesized nanoscopic gold particles: Optical spectra and the effects of particle size and shape. *J. Phys. Chem.* **1994**, *98*, 2963-2971.
15. Lee, W.; Park, S.-J. Porous anodic aluminum oxide: Anodization and templated synthesis of functional nanostructures. *Chem. Rev.* **2014**, *114*, 7487-7556.

16. Lee, J.; Mubeen, S.; Ji, X.; Stucky, G. D.; Moskovits, M. Plasmonic photoanodes for solar water splitting with visible light. *Nano Lett.* **2012**, *12*, 5014-5019.

17. Sobhani, A.; Manjavacas, A.; Cao, Y.; Mcclain, M. J.; García De Abajo, F. J.; Nordlander, P.; Halas, N. J. Pronounced linewidth narrowing of an aluminum nanoparticle plasmon resonance by interaction with an aluminum metallic film. *Nano Lett.* **2015**, *15*, 6946-6951.

18. Mock, J. J.; Hill, R. T.; Degiron, A.; Zauscher, S.; Chilkoti, A.; Smith, D. R. Distance-dependent plasmon resonant coupling between a gold nanoparticle and gold film. *Nano Lett.* **2008**, *8*, 2245-2252.

19. Albella, P.; et al. Shape matters: Plasmonic nanoparticle shape enhances interaction with dielectric substrate. *Nano Lett.* **2011**, *11*, 3531-3537.

20. Lévêque, G.; Martin, O. J. F. Optical interactions in a plasmonic particle coupled to a metallic film. *Opt. Express* **2006**, *14*, 9971-9981.

21. Nordlander, P.; Prodan, E. Plasmon hybridization in nanoparticles near metallic surfaces. *Nano Lett.* **2004**, *4*, 2209-2213.

22. Le, F.; Lwin, N. Z.; Steele, J. M.; Käll, M.; Halas, N. J.; Nordlander, P. Plasmons in the metallic nanoparticle−film system as a tunable impurity problem. *Nano Lett.* **2005**, *5*, 2009-2013.

23. Evans, P. R.; Kullock, R.; Hendren, W. R.; Atkinson, R.; Pollard, R. J.; Eng, L. M. Optical transmission properties and electric field distribution of interacting 2d silver nanorod arrays. *Adv. Funct. Mater.* **2008**, *18*, 1075-1079.

24. Wurtz, G. A.; Dickson, W.; O'connor, D.; Atkinson, R.; Hendren, W.; Evans, P.; Pollard, R.; Zayats, A. V. Guided plasmonic modes in nanorod assemblies: Strong electromagnetic coupling regime. *Opt. Express* **2008**, *16*, 7460-7470.

25. Lee, A.; Ahmed, A.; Dos Santos, D. P.; Coombs, N.; Park, J. I.; Gordon, R.; Brolo, A. G.; Kumacheva, E. Side-by-side assembly of gold nanorods reduces ensemble-averaged sers intensity. *J. Phys. Chem. C* **2012**, *116*, 5538-5545.

26. Prodan, E.; Radloff, C.; Halas, N. J.; Nordlander, P. A hybridization model for the plasmon response of complex nanostructures. *Science* **2003**, *302*, 419-422.

27. Nordlander, P.; Oubre, C.; Prodan, E.; Li, K.; Stockman, M. Plasmon hybridization in nanoparticle dimers. *Nano Lett.* **2004**, *4*, 899-903.

28. Willingham, B.; Brandl, D.; Nordlander, P. Plasmon hybridization in nanorod dimers. *Appl. Phys. B: Lasers Opt.* **2008**, *93*, 209-216.

29. Evans, P.; Hendren, W.; Atkinson, R.; Wurtz, G.; Dickson, W.; Zayats, A.; Pollard, R. Growth and properties of gold and nickel nanorods in thin film alumina. *Nanotechnology* **2006**, *17*, 5746.

30. Atkinson, R.; Hendren, W. R.; Wurtz, G. A.; Dickson, W.; Zayats, A. V.; Evans, P.; Pollard, R. J. Anisotropic optical properties of arrays of gold nanorods embedded in alumina. *Phys. Rev. B* **2006**, *73*, 235402.

31. Evans, P. R.; Wurtz, G. A.; Atkinson, R.; Hendren, W.; O'connor, D.; Dickson, W.; Pollard, R. J.; Zayats, A. V. Plasmonic core/shell nanorod arrays: Subattoliter controlled geometry and tunable optical properties. *J. Phys. Chem. C* **2007**, *111*, 12522-12527.

32. Fiehler, V.; Patrovsky, F.; Ortmann, L.; Derenko, S.; Hille, A.; Eng, L. M. Plasmonic nanorod antenna array: Analysis in reflection and transmission. *J. Phys. Chem. C* **2016**, *120*, 12178-12186.

33. Jiang, R.; Li, B.; Fang, C.; Wang, J. Metal/semiconductor hybrid nanostructures for plasmon-enhanced applications. *Adv. Mater.* **2014**, *26*, 5274-5309.

34. Johnson, P. B.; Christy, R. W. Optical constants of the noble metals. *Phys. Rev. B* **1972**, *6*, 4370-4379.

35. Masuda, H.; Satoh, M. Fabrication of gold nanodot array using anodic porous alumina as an evaporation mask. *Jpn. J. Appl. Phys.* **1996**, *35*, L126.

36. Krismastuti, F. S. H.; Bayat, H.; Voelcker, N. H.; Schönherr, H. Real time monitoring of layer-by-layer polyelectrolyte deposition and bacterial enzyme detection in nanoporous anodized aluminum oxide. *Anal. Chem.* **2015**, *87*, 3856-3863.

37. Thibaut, T.; Yuanhui, Z.; Hock, N. S.; Stephen, M.; Matteo, A.; Udo, B. Self-assembly of vertically aligned gold nanorod arrays on patterned substrates. *Angew. Chem., Int. Ed.* **2012**, *51*, 8732-8735.

38. López-Pastrana, M. A.; Ortega-López, M.; Matsumoto, Y. Vertically aligned zno nanorod arrays grown by chemical bath deposition on bare- and ito-coated glass substrates. *In: 2016 13th International Conference on Electrical Engineering, Computing Science and Automatic Control (CCE)*, 26-30 Sept. 2016, 2016, pp.1-5.

39. Lermé, J.; Bonnet, C.; Broyer, M.; Cottancin, E.; Manchon, D.; Pellarin, M. Optical properties of a particle above a dielectric interface: Cross sections, benchmark calculations, and analysis of the intrinsic substrate effects. *J. Phys. Chem. C* **2013**, *117*, 6383-6398.

40. Zhang, J. Z.; Noguez, C. Plasmonic optical properties and applications of metal nanostructures. *Plasmonics* **2008**, *3*, 127-150.

41. Liang, Y.; Zhen, C.; Zou, D.; Xu, D. Preparation of free-standing nanowire arrays on conductive substrates. *J. Am. Chem. Soc.* **2004**, *126*, 16338-16339.

42. Park, J. E.; Kim, M.; Hwang, J. H.; Nam, J. M. Golden opportunities: Plasmonic gold nanostructures for biomedical applications based on the second near-infrared window. *Small Methods* **2017**, *1*, 1600032.

43. Ciracì, C.; Hill, R. T.; Mock, J. J.; Urzhumov, Y.; Fernández-Domínguez, A. I.; Maier, S. A.; Pendry, J. B.; Chilkoti, A.; Smith, D. R. Probing the ultimate limits of plasmonic enhancement. *Science (New York, N.Y.)* **2012**, *337*, 1072-1074.

44. Osberg, K. D.; Harris, N.; Ozel, T.; Ku, J. C.; Schatz, G. C.; Mirkin, C. A. Systematic study of antibonding modes in gold nanorod dimers and trimers. *Nano Lett.* **2014**, *14*, 6949-6954.

45. Jain, P. K.; Eustis, S.; El-Sayed, M. A. Plasmon coupling in nanorod assemblies: Optical absorption, discrete dipole approximation simulation, and exciton-coupling model. *J. Phys. Chem. B* **2006**, *110*, 18243-18253.

46. Gans, R. Über die form ultramikroskopischer goldteilchen. *Ann. Phys.* **1912**, *342*, 881-900.

47. Morgan, F.; Murphy, A.; Hendren, W.; Wurtz, G.; Pollard, R. J. In situ ellipsometric monitoring of gold nanorod metamaterials growth. *ACS Appl. Mater. Interfaces* **2017**, *9*, 17379-17386.

8. AUTHOR INFORMATION

* Dr Joshua William Cottom

Research Fellow at the University of Leeds,

School of Chemical and Process Engineering,

University of Leeds, LS2 9JT, UK.

J.W.Cottom@leeds.ac.uk

+44 (0) 7791 657 094

9. TOC GRAPHIC